Catalysis Today 169 (2011) 207–216

Contents lists available at ScienceDirect

Catalysis Today

journal homepage: www.elsevier.com/locate/cattod

The mechanism of the reaction of intradiol dioxygenase with hydroperoxy probe A DFT study

Anna Wójcik, Tomasz Borowski *, Ewa Broclawik

Institute of Catalysis and Surface Chemistry, Polish Academy of Sciences, Niezapominajek 8, 30-239, Kraków, Poland

ARTICLE INFO

Article history:
Available online 14 November 2010

Keywords:
Intradiol
Extradiol
Dioxygenase
Non-heme
Iron
Reaction mechanism
DFT

ABSTRACT

The mechanism for the reaction between an intradiol dioxygenase and a hydroperoxy probe was modeled with the DFT method – B3LYP. Five models of the iron cofactor – probe complexes differing in the total charge and the number of ligands bound to iron were considered. The most important conclusion from the study described in this contribution is that the critical O–O bond cleavage, leading to the alkoxyl radical intermediate, most likely does not yield the reactive oxoferryl species. Instead, in the preferred reaction channel the peroxo group is protonated and the O–O cleavage leads to the ferrous complex with one of the tyrosine ligands oxidized to the tyrosinate radical. The factors affecting the product specificity are also discussed in the paper.

1. Introduction

Intradiol dioxygenases belong to the group of enzymes responsible for biodegradation of aromatic compounds originating from natural (lignin) or anthropogenic sources [1,2]. They are non-heme Fe(III)-dependent dioxygenases found in soil bacteria that catalyze oxidative cleavage of catecholic substrates (Fig. 1).

These enzymes are called *intradiol*, since they specifically cleave the aromatic ring between the two carbon atoms bound to hydroxyl groups, as depicted in Fig. 1, whereas the dioxygenase nature of these biocatalysts manifests in that two oxygens originating from O_2 are incorporated into the product, one in each COOH group formed in the reaction [3]. Intradiol dioxygenases that have been identified so far process either catechol (R=H) or protocatechuate ($R=COO^-$) substrates, and hence they are called either catechol or protocatechuate dioxygenases, abbreviated hereafter to CatA and PCD, respectively.

Crystal structures were solved for CatA [4] and PCD [5], and they revealed that both types of intradiol dioxygenases have very similar architecture of the active site, and thus, presumably also the same mechanism of the catalytic cycle. In the resting state, represented by structure **a** in Fig. 2, the ferric ion is coordinated by five ligands arranged in the trigonal bipyramid geometry. In the equatorial plane there are two protein ligands, namely imidazole side chains of histidine (His) and phenolate of tyrosine residue (Tyr). The third ligand in the plane is a hydroxyl group derived from the solvent. The two axial positions are occupied by another His–Tyr pair.

Crystal structures solved for wild type and several point mutants of PCD complexed with organic substrate [6] or its various analogues [7] provided detailed insights into the early stages of the catalytic cycle. More specifically, it was shown that during the substrate binding it is the OH ligand that abstracts the first proton from the catechol. The second proton is transferred from the catechol to the axial Tyr ligand, and both water and axial tyrosine dissociate from the metal making space for the dianion of the substrate, which chelates Fe(III) with its both oxygens, as represented by the species **b** in Fig. 2. The fact that it is a doubly ionized catechol that binds to iron was confirmed with spectroscopic methods [8,9]. Experimental evidence concerning the mechanism of the catalytic steps following substrate binding is scarce. Spectroscopic measurements under turnover conditions indicate that no stable species with oxidation state different from Fe(III) can be observed [9,10]. Therefore, the mechanistic proposals for transformation of **b** to **f** (Fig. 2) are based either on quantum chemical studies [11] or deduced from indirect experimental works [12]. Thus, it was suggested that binding of dioxygen leads to species with a peroxide bridge between the ferric ion and catechol substrate, as shown for species **c** in Fig. 2. DFT[11] and CASSCF/CASPT2 [13] calculations indicated that at the initial stage of O_2 binding, dioxygen molecule is one-electron reduced by the catecholate ligand, and the thus formed superoxide radical anion interacts with Fe(III). In the subsequent step, superoxide and catecholate radicals recombine forming peroxo species **c**. Since in this step one of the phenolic bonds of the substrate becomes a ketone group, which is a much weaker ligand, species **c** can easily change its conformation. This change opens a coordination site

* Corresponding author.
E-mail address: ncborows@cyf-kr.edu.pl (T. Borowski).

0920-5861/$ – see front matter © 2010 Elsevier B.V. All rights reserved.
doi:10.1016/j.cattod.2010.08.028

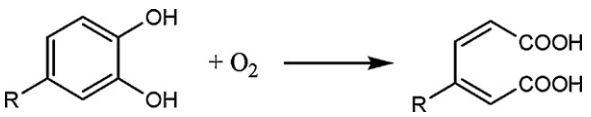

Fig. 1. Reaction catalyzed by intradiol dioxygenases. R=H or COO^-.

originally occupied by the axial tyrosine and thus, allows the tyrosine to return to the coordination sphere of iron[11]. The tyrosine binds to Fe(III) as a phenolate, whereas the proton is either released from the active site (**c** → **d**)[12], or it neutralizes the peroxide ligand (**c** → **d′**)[11].

In this first scenario, where the proton is released, the O–O bond cleavage yields species **e** which features a reactive oxoferryl group and an alkoxyl radical[12]. An attack of the oxyl radical on the adjacent carbonyl carbon, followed by ring expansion and protonation of the oxo ligand leads to the species **f**, where muconic anhydride is loosely bound to the metal. Plain hydrolysis of the anhydride, e.g. by the Fe(III)-bound OH ligand, leads to the final reaction product – muconic acid. Such a reaction mechanism, involving formation of oxoferryl species, has recently been confirmed in computational studies on synthetic complex catalyzing intradiol type cleavage [14]. Interestingly the reaction path with the lowest activation barrier lies on a quartet potential energy surface, which is a low lying excited state.

In the second scenario, which assumes the proton remains in the active site, the peroxide oxygen atom which is proximal with respect to Fe(III) is protonated. This fact prevents oxidation of iron to a high-valent Fe(IV)=O state during the O–O bond cleavage[11]. As a result, species **d′** either undergoes a Criegee rearrangement (**d′** → **f**), which involves concerted O–O bond heterolysis and migration of the acyl group to the peroxide oxygen, or it evolves towards the muconic anhydrate product via O–O bond cleavage facilitated by the equatorial tyrosine, which is transiently oxidized to a tyrozyl radical (**d′** → **e′**). An attack of the oxyl radical on the carbonyl carbon is coupled with reduction of the tyrozyl radical to tyrosinate (**e′** → **f**).

The first mechanism (**c** → **d** → **e** → **f**) has recently been proposed by Xin and Bugg based on their experimental findings obtained for 2-hydroperoxy-2-methylocyklohexanone (**A** in Fig. 3), which is a mechanistic probe reacting with intradiol dioxygenase[12]. Upon incubation of **A** with the enzyme (CatA), 5,6-diketoheptan-1-ol (**F**) was obtained as a reaction product, and to explain this observation the mechanism presented in Fig. 3 was proposed.

According to this mechanistic hypothesis, the probe molecule (**A**) binds to the iron ion in the active site and, after releasing the proton, the O–O bond is cleaved homolitically producing alkoxide radical species **B** and the oxoferryl (Fe^{IV}=O) form of the metal cofactor. The reactive radical **B** can in principle decay via two pathways. First, homolysis of the C–C bond joining the carbonyl group with the radical-bound carbon (**B** → **C**) yields a more stable radical (**C**), which is quenched by the oxoferryl species (**C** → **D**) producing the keto-acid product **D**. Second, cleaving the other C–C bond in the ring (**B** → **E**) leads to alkyl radical intermediate **E**, which by reacting with the oxoferryl form of the iron cofactor forms the experimentally observed product **F**. Interestingly, even though **C** is expected to be thermodynamically more stable than **E**, product **D** was not detected. Therefore, the probe **A** is an interesting new substrate for intradiol dioxygenases which reacts in a way suggesting par-

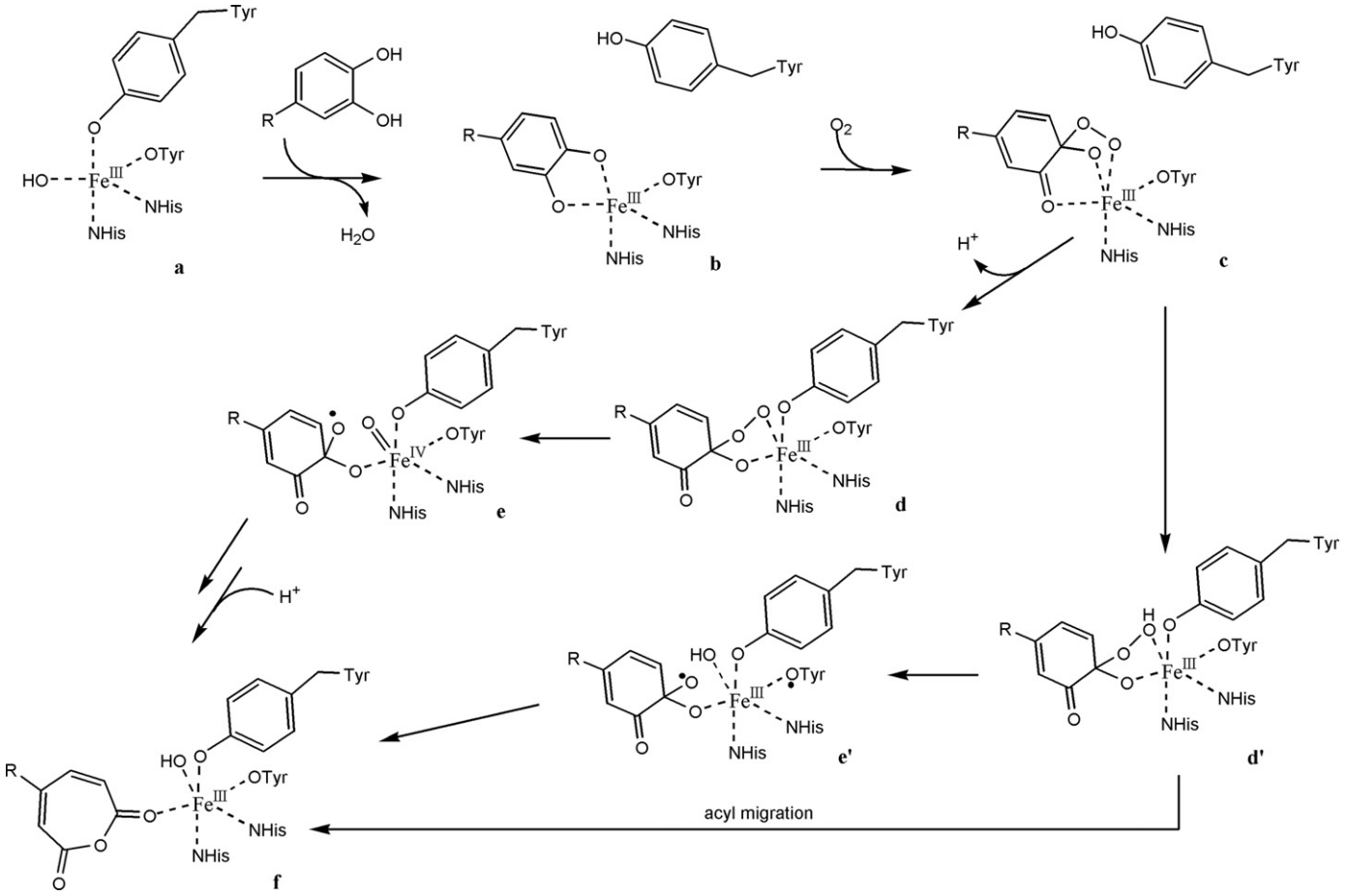

Fig. 2. Suggested mechanisms for catalytic reaction of intradiol dioxygenases.

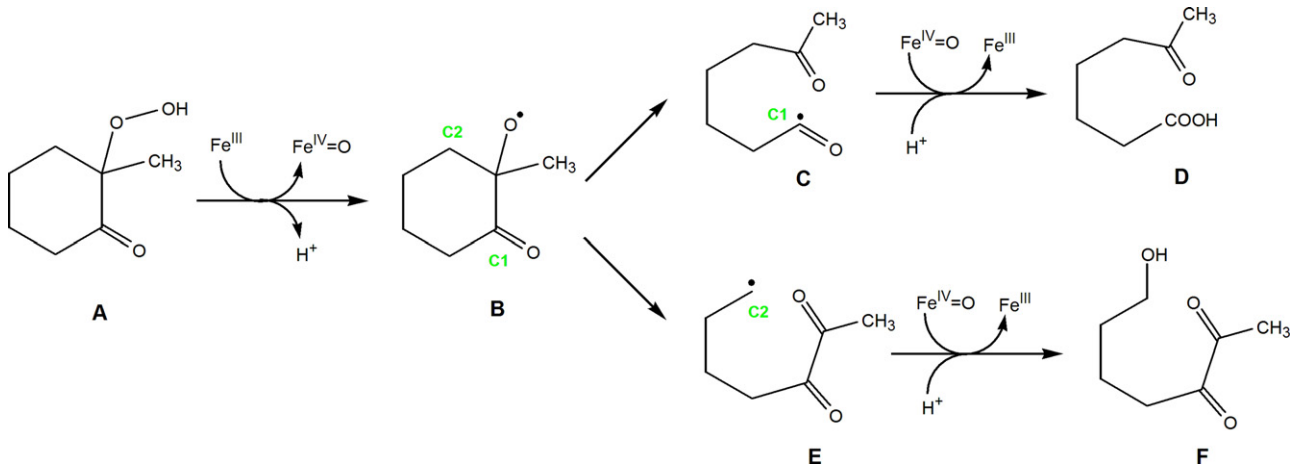

Fig. 3. Suggested reaction mechanism for the mechanistic probe **A** and intradiol dioxygenases[12].

ticipation of radical species in the reaction mechanism. Since it is currently neither known if the probe is deprotonated upon binding to the active site, nor if the second tyrosine remains bound to iron in the presence of the probe, we undertook a DFT study with the hope to elucidate the influence of these factors on the reaction mechanism.

In this work we studied, by means of theoretical methods, the reaction mechanism for intradiol dioxygenase reacting with the mechanistic probe **A** (Fig. 3). The reaction pathways leading to the two expected products, i.e. **F** and **D**, were characterized for five models of the active site. The models differ in the protonation state of the peroxo group and the presence or absence of the axial tyrosine residue and the OH ligand, which are known to dissociate from the metal when the native substrate binds to the active site (Fig. 2). The results reported below show that the protonation state of the peroxo group has a substantial influence on the mechanism and the barrier for O–O bond cleavage.

2. Methodology

2.1. Computational details

All calculations were performed using density functional theory (DFT) method with a hybrid exchange correlation functional-B3LYP [15,16]. Geometry optimizations were performed with two programs, Jaguar [17] and Gaussian [18], employing a double-ζ basis set, available in the Jaguar package under a *lacvp* acronym. For the optimized structures electronic energy was computed with triple-ζ basis set combining *cc-pVTZ*(−*f*) basis for H,C,N and O atoms, and *lacv3p* + basis for iron. Gaussian program was also used to calculate molecular vibrations, analysis of which was used to validate the character of the optimized stationary point. The solvent effects, due to the surrounding protein, were computed with the self-consistent reaction field method implemented in Jaguar [19,20]. The protein was treated as a macroscopic continuum with a dielectric constant of 4.0, and the solute cavity was obtained with a probe radius of 1.4 Å.

2.2. Models

The active site models employed in this work were constructed from the model used in previous investigations on the reaction mechanism of intradiol dioxygenases[11]. To this end, catechol, i.e. the native substrate, was replaced with the probe molecule **A**. The model was based on crystal structure of protocatechuate 3,4-dioxygenase (PDB code: 3PCL), which reveals that in the substrate-free form the iron cofactor adopts a trigonal bipyramidal structure [5]. In the equatorial plane there are tyrosinate (Tyr408), histidine (His460) and the solvent derived OH group. Another tyrosinate (Tyr447) and histidine (His462) are placed in axial positions. In our models histidines were truncated to methylimidazoles, and tyrosine residues to 4-methylphenol anion (Tyr408) and phenol anion (Tyr447). Tyr408, which is a mobile residue, was not constrained, whereas for His460, His462 and Tyr408 models the positions of hydrogens and carbons replacing Cα and Cβ were constrained during optimizations. In this way the rigidity of the protein backbone was incorporated into the computational model in an approximate way.

Concerning the structure of the active site in the enzyme-probe complex, it is important to note that at present there is no experimental data providing information on how the probe **A** binds to the metal cofactor. Specifically, it is not known if the mobile tyrosine remains bound to the metal, and also if the peroxo group of the probe remains protonated when binding to Fe. For these reasons five different models of the first coordination sphere of iron were considered in the calculations. They differ in the presence or absence of the second tyrosine residue and the OH ligand, and in the protonation state of the peroxo group (Figs. 4 and 5).

The model I can be considered as derived from the native enzyme-substrate complex by replacing the dianionic catecholate with the charge-neutral probe **A**. Thus, the total charge of the model I is +2, as opposed to the native enzyme-substrate complex, which has a total charge of 0. Moreover, the native substrate displaces OH and axial tyrosine (Tyr447) from the iron first coordination sphere and thus, those ligands are also absent in the model I. On the other hand, a model where both OH and Tyr447 ligands remain bound to iron is the model III. In this case, the probe molecule binds in the sixth coordination site of Fe(III) and the total charge of the active site, amounting to 0, is preserved upon binding of **A**. Similarly charge-neutral is the model II, which is formed from the model III by a transfer of a proton from the hydroperoxo group of the probe to the OH ligand, which leaves the coordination sphere of iron as water molecule. The calculated reaction energy for such a proton transfer is −3.2 kcal/mol, which reflects the larger acidity of the hydroperoxide compared to water. Besides those two limiting cases, represented by the models I and II (or III), two other models were considered. In one of them, called the model IV, the OH and Tyr447 ligands are replaced with a deprotonated form of the probe. The total charge of the model IV is +1. The same total charge features the model V, where the charge-neutral probe replaces the OH ligand, but Tyr447 remains bound to iron.

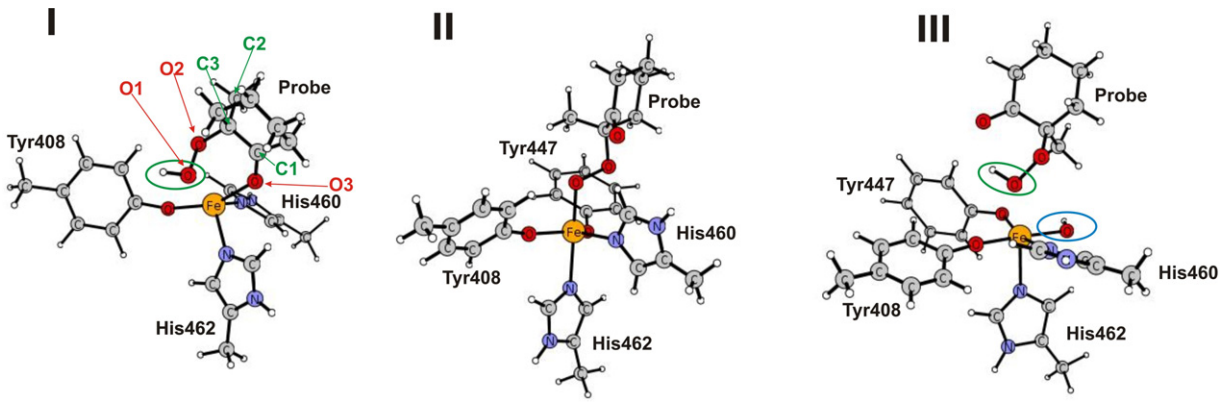

Fig. 4. The optimized structures for the models I, II and III of the enzyme-probe complex.

3. Results and discussion

The reaction of the mechanistic probe **A** in the active site of intradiol dioxygenase was modeled for two spin states: sextet, which is a ground electronic state for all local minima on the reaction path, and quartet, which is a low lying excited state with calculated electronic energy at most 15 kcal/mol higher.

The reaction paths leading from **A** to **D** or **F** (Fig. 3) were modeled employing the five models depicted in Figs. 4 and 5. Below we discuss in detail the results obtained for the two limiting cases represented by the models I and II, which differ the most in terms of the total charge, protonation state of the peroxo group and the presence of the Tyr447 in the coordination sphere. Model V, which gave barriers only slightly higher than model I is also discussed in detail, though the reaction mechanisms found for these two models are basically identical. Results for the models III and IV resemble one of the two limiting cases, and thus are only briefly summarized at the end of this section. Moreover, only the results obtained for the sextet ground state are presented because the quartet stationary points lie higher in energy than the sextet counterparts.

3.1.1. Model I

The key intermediates for the reaction of **A** in the active site of intradiol dioxygenase, as modeled with the model I, are presented in Fig. 6, whereas the corresponding energy profile is shown in Fig. 7. The first distinctive feature of the presented mechanism is the fact that the tyrozyl ligand is oxidized to a tyrozyl radical in all of the structures along the reaction paths. This is caused by the fact that the probe molecule is charge-neutral, whereas the native catechol binds to the iron as a dianion, and this extra negative charge stabilizes the ferric oxidation state. Thus, in the reactant enzyme-probe complex **R1** (Fig. 6 and Table 1) a high-spin Fe(II) is bound to the tyrozyl radical, while the probe molecule forms two coordination bonds to the metal. The spin populations reported in the Table 1 are consistent with this assignment of oxidation states, with the value of 3.8 typical for high-spin Fe(II).

The suggested reaction mechanism involves two major steps. The first is a homolytic cleavage of the O–O bond leading to the alkoxyl radical **R2**, which is a common intermediate for the two reaction paths leading to either **R3** or **R5**. The second major step involves homolytic C–C bond cleavage in **R2**, which depending on the cleavage site eventually leads to **R3** or **R5**. The cleavage of the C–C bond between the two carbons bound to oxygen atoms will be called “intradiol cleavage”, whereas the alternative is termed “extradiol cleavage”.

With respect to the O–O cleavage, this step involves a barrier of 12.9 kcal/mol connected with the transition state **Ts1** (Figure S1b). Comparing the structures of **R1** and **Ts1** one can notice that the hydroxide group which forms in the cleavage process binds to iron, and similarly the oxygen which becomes a radical center establishes a contact with the metal. For **Ts1** the distances between iron and these two oxygen atoms, labeled O1 and O2 in Table 1 and Figure S1, are 2.01 and 2.13 Å, respectively. For this transition state the O–O bond is stretched to 1.81 Å, and from the spin populations it can be recognized that the cleavage is coupled to oxidation of Fe(II) to Fe(III). Indeed, little spin builds on O1, whereas the spin population on iron monotonically increases in the sequence **R1** → **Ts1** → **R2** to the value of 4.08 for **R2**, which is typical for high-spin Fe(III) (Table 1).

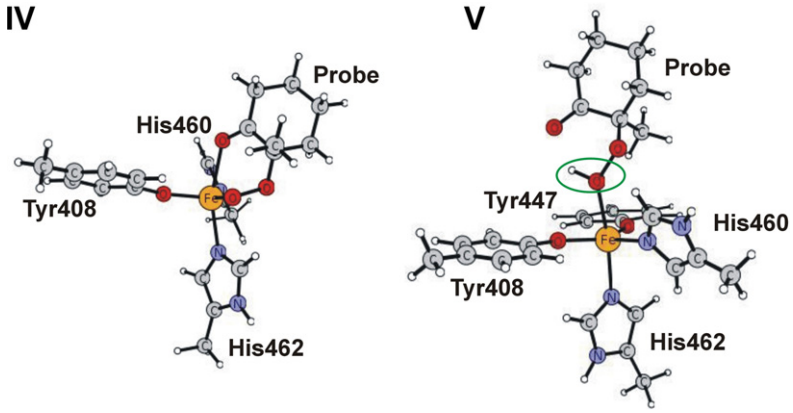

Fig. 5. The optimized structures for the models IV and V of the enzyme-probe complex.

Table 1
Spin populations and the most important distances of the optimized structures of intermediates and transition states involved in reaction paths for models I, II and V. The distances (Å) are labeled with "d" and spin populations with "s".

Species	dFe–O1 (Å)	dFe–O2 (Å)	dFe–O3 (Å)	dO1–O2 (Å)	dC1–C3 (Å)	dC2–C3 (Å)	dFe–Tyr408 (Å)	dO1–C2	dO1–C1 (Å)	dFe–Tyr447	sFe	sO1	sO2	sC1	sC2	sTyr408	sTyr447
MODEL I																	
R1	2.30	2.58	2.15	1.54	1.53	1.54	1.95	2.97	2.84	–	3.81	0.00	0.00	0.00	0.00	0.92	–
Ts1	2.01	2.13	2.17	1.81	1.53	1.55	2.03	3.12	2.92	–	3.94	0.08	−0.33	0.00	0.00	1.02	–
R2	1.82	2.18	2.23	2.88	1.54	1.61	2.06	3.62	3.41	–	4.08	0.43	−0.68	0.00	0.00	1.08	–
Ts2p1	1.86	2.03	3.04	2.74	2.41	1.52	2.00	3.17	3.21	–	4.02	0.00	0.37	−0.40	0.00	1.08	–
R3	3.59	2.21	2.13	3.68	3.34	1.51	1.94	3.75	1.36	–	3.81	0.00	0.00	0.00	0.00	1.20	–
Ts2p2	1.85	2.14	2.24	2.82	1.52	2.35	2.06	3.22	3.41	–	4.09	0.40	−0.18	0.00	−0.61	1.09	–
R4	1.85	2.17	2.22	2.85	1.52	2.66	2.07	3.29	3.46	–	4.02	0.41	0.00	0.00	−0.71	1.09	–
Ts3p2	1.87	2.26	2.13	2.78	1.52	3.57	1.96	2.61	3.11	–	4.01	0.36	0.00	0.00	−0.62	1.04	–
R5	2.28	2.26	2.28	2.86	1.54	4.13	1.96	1.50	2.76	–	3.84	0.00	0.00	0.00	0.00	1.04	–
MODEL II																	
RI	1.95	2.87	4.71	1.52	1.54	1.56	1.87	3.72	3.09	1.88	3.96	0.30	0.00	0.00	0.00	0.29	0.29
TsI	1.68	3.71	4.54	2.12	1.54	1.57	1.87	4.26	3.42	1.87	3.24	0.45	0.81	0.00	0.00	0.18	0.17
RII	1.66	5.32	4.70	4.32	1.54	1.58	1.87	5.46	3.64	1.87	2.98	0.62	0.90	0.00	0.00	0.18	0.14
TsIIp1	1.66	6.45	5.25	5.94	2.06	1.54	1.87	7.30	4.81	1.89	2.99	0.65	0.36	0.35	0.00	0.13	0.14
RIII	1.66	6.51	5.01	6.03	2.84	1.52	1.86	5.01	4.50	1.89	2.98	0.66	0.05	0.60	0.00	0.13	0.14
TsIIp2	1.66	4.96	4.33	3.82	1.54	2.20	1.86	5.13	2.81	1.88	3.00	0.61	0.39	0.00	0.01	0.19	0.12
RIV	1.66	4.65	4.30	3.41	1.55	3.37	1.86	5.57	2.68	1.88	3.00	0.61	0.01	0.00	1.06	0.18	0.12
MODEL V																	
M1	2.27	3.57	4.53	1.53	1.54	1.55	1.85	3.77	2.91	1.84	3.91	0.00	0.00	0.00	0.00	0.46	0.44
TM1	1.95	3.68	4.24	1.94	1.54	1.57	2.02	4.14	3.06	1.84	3.92	0.19	−0.56	0.00	0.00	0.82	0.46
M2	1.85	4.06	4.44	2.47	1.54	1.57	2.12	4.60	3.33	1.86	3.94	0.23	−0.83	0.00	0.00	0.97	0.54
TM2	1.86	5.78	4.46	4.92	1.54	2.24	2.08	5.24	5.17	1.88	3.96	0.35	−0.35	0.00	−0.70	0.94	0.56
M3	1.86	5.72	4.37	4.86	1.55	3.08	2.09	5.64	4.22	1.87	3.96	0.36	0.00	0.00	−0.98	0.96	0.54
TM3	1.88	5.87	4.49	4.90	1.54	4.34	1.84	2.95	4.99	2.05	3.94	0.42	0.00	0.00	−0.95	0.42	0.91
M4	2.21	5.83	4.39	4.55	1.54	4.33	1.85	1.47	3.36	1.84	3.94	0.00	0.00	0.00	0.00	0.40	0.45
TMII	1.84	4.57	4.64	3.28	2.06	1.54	2.17	5.27	3.68	1.86	3.94	0.37	−0.38	−0.38	0.00	0.98	0.51
MIII	1.85	6.76	4.31	6.22	5.60	1.52	1.85	6.64	3.94	2.12	3.94	0.38	0.00	−0.68	0.00	0.52	1.00
TMIII	1.86	6.61	3.94	6.07	5.58	1.52	1.83	6.32	3.36	2.16	3.94	0.35	0.00	−0.58	0.00	0.47	1.13
MIV	1.88	6.57	4.06	4.97	5.78	1.52	1.83	5.48	3.66	2.34	3.96	0.29	0.00	0.00	0.00	0.52	0.04
TMIV	1.98	5.71	3.78	4.67	5.61	1.52	1.83	5.23	2.01	2.10	3.96	0.16	0.00	−0.01	0.00	0.58	0.08
MV	3.29	6.11	4.74	4.56	5.54	1.52	1.86	5.16	1.38	1.84	3.87	0.00	0.00	0.00	0.00	0.32	0.62

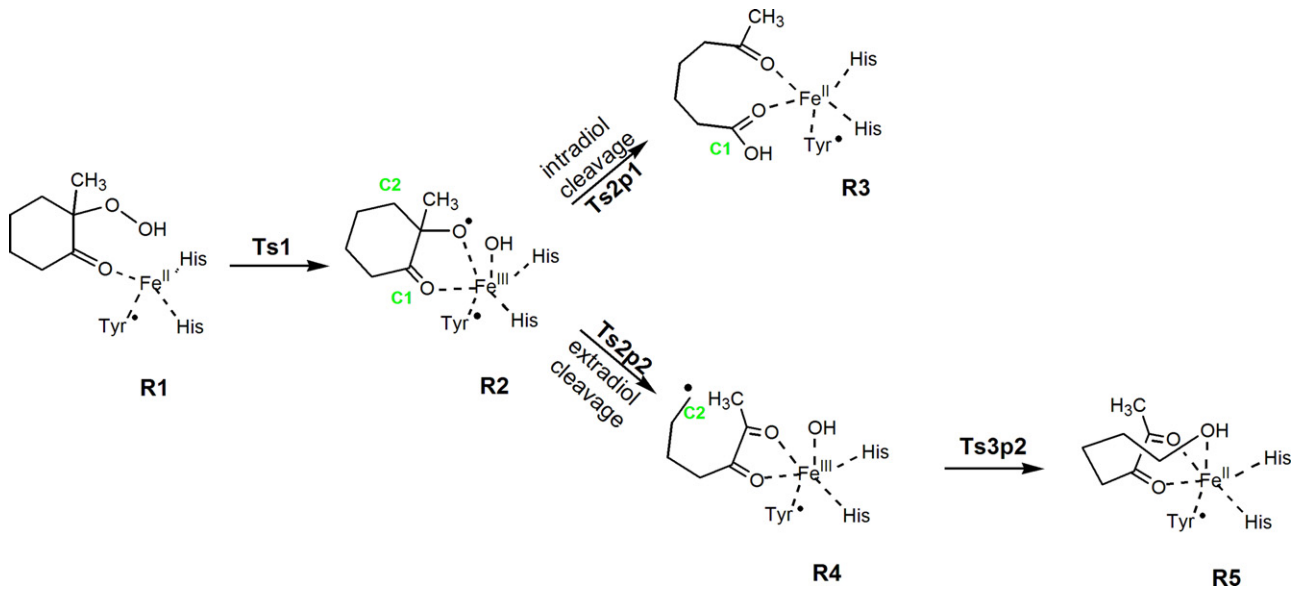

Fig. 6. Mechanism for the catalytic reaction of intradiol dioxygenases with the mechanistic probe **A**, as derived from the study for the model I.

The product of O–O bond cleavage, i.e. **R2**, is by 8.5 kcal/mol more stable than the reactant complex **R1** (Fig. 7), and as can be noticed in Table 1, it features an alkoxyl radical chelating Fe(III) with its carbonyl and oxyl groups. The OH ligand produced in the cleavage is also bound to the metal ion with a distance of 1.82 Å, typical for a Fe^{III}–OH bond. This intermediate (**R2**) is a branching point for the two reaction paths leading to **R3** or **R5** (Fig. 6). From Figs. 6 and 7 it follows that the *intradiol*-type cleavage effectively proceeds without a barrier, since the energy of the transition state **Ts2p1** is lowered below the level of **R2** when big basis and solvent corrections are applied. Thus the *intradiol* cleavage is predicted to proceed without a barrier, and this fact is at least partially explained by the higher stability of the radical product obtained in such a cleavage (the relative energies of **B**, **C** and **D**, shown in Fig. 3, are 0.0, −4.5 and +6.0 kcal/mol, respectively). In the presence of the metal cofactor (Fe^{III}–OH), the radical **C** is not a stable species as it is spontaneously trapped by the hydroxyl ligand forming the product complex **R3** (Fig. 6). Structures of both transition state (**Ts2p1**) and the product of the intradiol cleavage (**R3**) are presented in Figure S2. One can notice there that for the transition state the C–C bond is elongated to 2.41 Å, and that the negative spin density is transferred from O2 to C1 while the C–C bond is cleaved. Moreover, in the product complex **R3**, the spin populations indicate that iron and tyrosine (Tyr408) are back in their initial oxidation states,

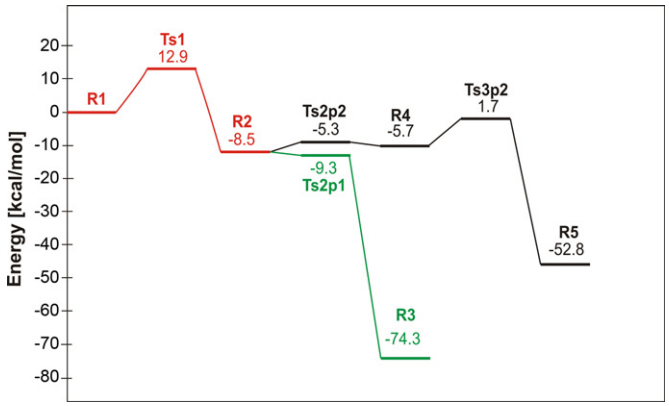

Fig. 7. Calculated energy profile for catalytic reaction of intradiol dioxygenases with the mechanistic probe **A**, as derived from the study for the model I.

whereas the organic product is in it ground closed-shell electronic configuration.

The alternative reaction of **R2** is the *extradiol*-type cleavage, which leads to the alkyl radical intermediate **R4** (Fig. 6). The calculated activation energy for this step is 3.2 kcal/mol and it is connected with a transition state **Ts2p2** presented in Figure S3.

In this transition state the dissociating C–C bond is stretched to 2.35 Å, and the beta spin population is transferred from O2 to C2, i.e. for **Ts2p2** the spin populations on O2 and C2 are −0.18 and −0.61, respectively. In the product of the cleavage, radical **R4**, the carbon which is the radical site is only 2.66 Å away from the newly formed carbonyl carbon, whereas the distance between this radical and the OH ligand is 3.29 Å. Shortening this distance to 2.61 Å leads to the final transition state on this reaction path, i.e. **Ts3p2** (Table 1, Figure S4a), whose calculated energy is 1.7 kcal/mol with respect to the reactant complex **R1**. In this step the alkyl radical combines with the OH ligand forming the product complex **R5** (Figure S4b), which features diketo-alcohol product coordinated to Fe(II), as can be inferred from the spin populations reported in Figure S4b and Table 1. In an attempt to find a lower barrier pathway leading from **R4** to **R5** a model with a water molecule placed between the radical site and the OH ligand was considered. For this model a transition state for an attack of the water molecule on the radical center, concerted with a proton transfer from H_2O to the OH iron ligand, was found, yet in this way the barrier was lowered by only 1 kcal/mol.

In sum, the results obtained for the model I show that if the peroxo group is protonated then the cleavage of the O–O bond is easy (12.9 kcal/mol barrier), the reactive oxoferryl species is not formed, and the preferred pathway for the decay of the alkoxyl radical intermediate **R2** leads to the intradiol cleavage product **R3**. This last observation stays in contrast with the experimental findings showing that **R5** is the sole reaction product[12]. However, the calculated barrier leading to **R5** is not very high, and since it is caused mostly by the strain, produced within the probe-derived ligand as it reaches for the OH group (compare Figures S3b and S4a), it seems likely that if the probe were bound slightly different this reaction channel might become competitive to the *intradiol* cleavage pathway.

3.1.2. Model II

The model II (Fig. 4) represents the second limiting case, where binding of the probe molecule causes little changes in the coordi-

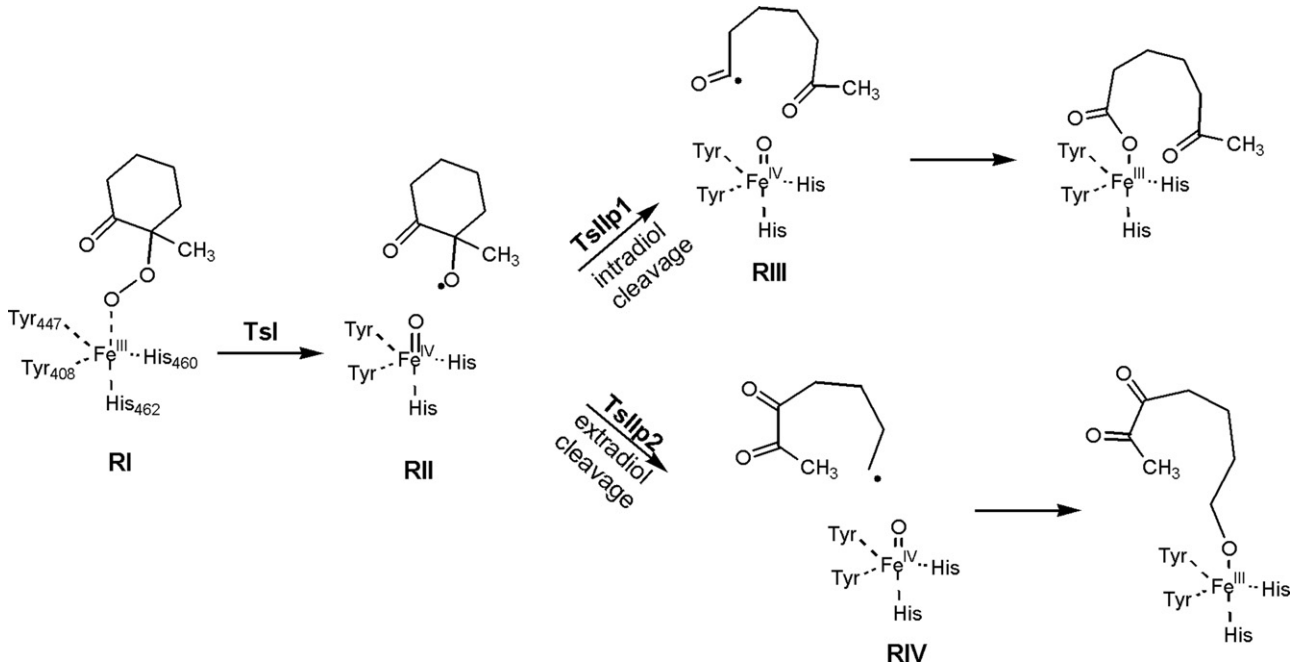

Fig. 8. Mechanism for the catalytic reaction of intradiol dioxygenases with the mechanistic probe **A**, as derived from the study for the model II.

nation sphere of iron. Likewise, the total charge, amounting to 0, is preserved upon substrate binding, since the OH ligand is replaced by the deprotonated probe. Interestingly, removing the proton form the peroxo group changes the mechanism of O–O bond cleavage. This can be noticed in Fig. 8, where the mechanism derived from computations for the model II is presented.

Thus, in the reactant complex **RI** a high-spin Fe(III) is coordinated by two tyrosinates, the deprotonated probe and the two histidines. The presence of three negatively-charged ligands stabilizes the ferric oxidation state of iron, which manifests in the spin population of 3.96 obtained for **RI** (Table 1, Figure S5a). The cleavage of the O–O bond involves a substantial activation barrier of 23.6 kcal/mol (Fig. 9) connected with the transition state **TsI** depicted in Figure S5b.

In this transition state the O–O bond is elongated to 2.12 Å, while the Fe–O1 bond is shorted to 1.68 Å, which indicates the oxoferryl species is formed in this step. Indeed, in the product of this step, i.e. **RII** presented in Figure S5c, the Fe–O1 bond has a length of 1.66 Å typical for oxoferryl species. From the spin populations one can recognize that, besides the Fe^{IV}=O form of the iron cofactor, the cleavage of the O–O bond affords the loosely bound alkoxyl radical with a radical center on O2 (Table 1, Figure S5c). The energy of **RII** calculated with respect to the reactant complex **RI** (Fig. 4S) is 17.0 kcal/mol, which clearly demonstrates the formation of the oxoferryl species in the intradiol dioxygenases is a difficult process,

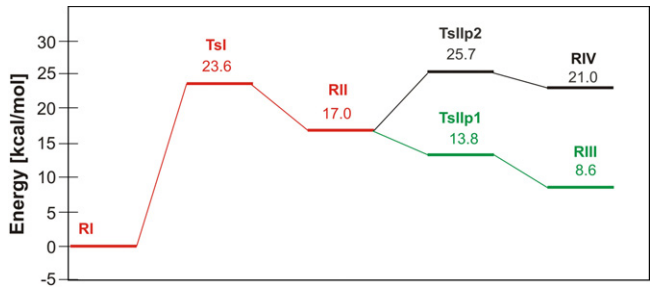

Fig. 9. Calculated energy profile for catalytic reaction of intradiol dioxygenases with the mechanistic probe **A**, as derived from the study for the model II.

at least in the reaction with the probe **A**.

Once the O–O bond is cleaved, the intra and extradiol cleavage reactions proceed in a similar manner as found for the model I. Accordingly, the intradiol cleavage is the favorable path for the decay of **RII** because there is no barrier along this path (Fig. 9). Like for the model I, the transition state connected with this type of cleavage was optimized (**TsIIp1**), yet when the big basis and solvent corrections were added, the barrier vanished completely. The product of this step, i.e. the intermediate **RIII** depicted in Figure S5b, features an acyclic radical with an unpaired electron delocalized between C1 and O3, as demonstrated by the spin populations of 0.60 and 0.24 for these two atoms. Concerning the energy, **RIII** is markedly more stable than **RII**, 8.6 vs 17.0 kcal/mol, which is understandable taking into account the larger stability of the –C•=O radical with respect to the parent R–O•. The following step of the intradiol path is expected to involve the attack of the oxo ligand (O1) on the radical carbon C1, and due to high reactivity of these two groups it is very unlikely that this final step has an activation barrier larger than 12.4 kcal/mol, which is an energy gap between **RIII** and **RIV** (Fig. 9). Thus, it follows that, like for the model I, the path leading to the intradiol product is a favorable reaction channel for the model II.

The alternative extradiol cleavage pathway involves an accumulated barrier of 25.7 kcal/mol (Fig. 9) connected with the transition state **TsIIp2** presented in Figure S7a.

In this transition state, where the cleaving C–C bond is elongated to 2.20 Å, the radical center is transferred from the oxygen O2 to the carbon C2. This is clearly evident from the spin populations reported for the product of this step, i.e. intermediate **RIV** (Table 1, Figure S7b), as the value for C2 is 1.06. The next step of the extradiol mechanism is expected to proceed with negligible barrier as the reactive aliphatic radical will be attacked by the oxoferryl group forming the alkoxide form of the extradiol reaction product.

Concluding the results obtained for the model II, when the peroxo group is not protonated, the cleavage of the O–O bond leads to the oxoferryl (Fe^{IV}=O) species and an alkoxyl radical derived from the probe (Fig. 8). However, the energy barrier for this step is rather high (23.6 kcal/mol), which together with the substantial energy (17.0 kcal/mol) calculated for the radical product

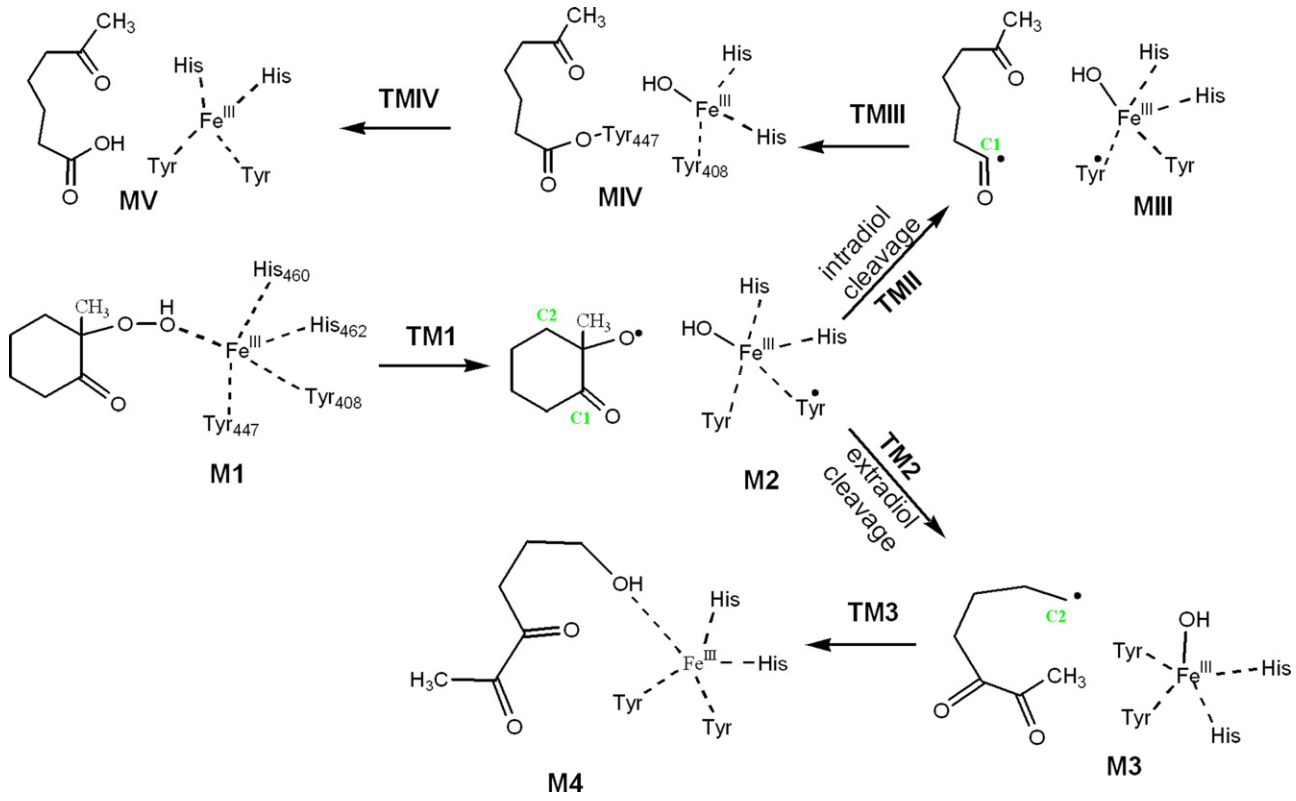

Fig. 10. Mechanism for the catalytic reaction of intradiol dioxygenases with the mechanistic probe **A**, as derived from the study for the model V.

indicates that such a process is rather difficult. Like for the model I, the preferred reaction channel leads to the intradiol cleavage products.

3.1.3. Model V

Model V represents the case where the Fe(III) is coordinated by two tyrosinates, two histidines and protonated probe bound to the metal by its peroxo group. The presence of the second tyrosinate (Tyr447) causes minor changes in the reaction path, which is presented in Fig. 10. Thus, the reaction begins with the homolytic cleavage of O–OH bond, which process involves a modest activation barrier of 14.6 kcal/mol (Fig. 11). The transition state connected

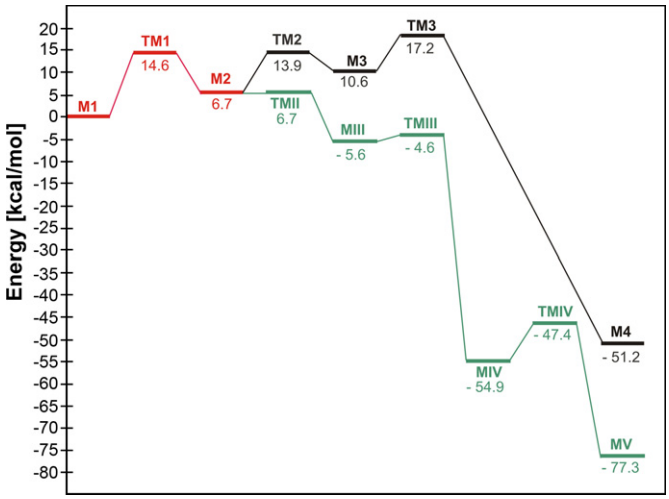

Fig. 11. Calculated energy profile for catalytic reaction of intradiol dioxygenases with the mechanistic probe **A**, as derived from the study for the model V.

with this step – **TM1** (Table 1) is presented in Figure S8b, where it can be noticed that the O–OH bond is stretched to 1.94 Å. With respect to the mechanism of this reaction, it can be recognized from the data in Table 1 that the O–OH bond homolysis is coupled with one-electron oxidation of one tyrosine ligand (Tyr408). Indeed, the total spin population on Tyr408 increases from 0.46 in **M1** to 0.82 in **TM1**, and then to 0.97 in **M2**, whereas the spin population on iron practically does not change.

The O–O bond cleavage product (**M2**) lies 6.7 kcal/mol higher in energy than the reactant complex **M1**, and it features an alkoxyl radical in the second coordination sphere of Fe(III). Mechanisms of the subsequent steps, which are intra or extradiol C–C bond cleavages, are similar to those found for models I and II. Accordingly, the intradiol cleavage path involves lower barrier than the extradiol one. The step involving intradiol C–C bond cleavage occurs without a barrier and leads to reaction complex **MIII** (Figure S9b) with radical centers on Tyr447 and carbon labeled as C1. The product of intradiol C–C bond cleavage, i.e. **MIII**, is by 12.3 kcal/mol more stable than the alkoxyl radical **M2**, and in its acyclic organic radical the distance between the carbons separated in the previous step equals to 5.78 Å. Interestingly, this **M2** → **MIII** transformation is accompanied by an electron transfer between two tyrosine ligands, as can be noticed from the changes in spin populations. The spin population on Tyr408 decreases from 0.97 to 0.52, whereas on Tyr447 it increases from 0.54 to 1.00 (Table 1).

As it can be noticed in Fig. 10, the next step on the intradiol reaction path is formation the ester **MIV** (Figure S10b), which is realized by an attack of the tyrozyl radical (Tyr447) on the radical carbon C1. This step involves the activation barrier of only 1 kcal/mol, connected with the transition state **TMIII** (Figure S10a), whose energy is −4.6 kcal/mol with respect to **M1** (Fig. 11). The resulting complex **MIV**, which involves the ester intermediate, is by 49.3 kcal/mol more stable than **MIII**. This intradiol reaction path finishes with the hydrolysis of the ester, which is elicited by the nucleophilic attack of the OH ligand on the carbonyl carbon of the ester group. The

Table 2
Activation barriers of three critical reaction steps for all models considered. The energies are given with respect to the preceding intermediate.

Model	O–O homolytic cleavage (kcal/mol)	C–C extradiol cleavage (kcal/mol)	C–C intradiol cleavage (kcal/mol)
Model I	12.9	3.2	0.0
Model II	23.6	8.7	0.0
Model III	15.9	9.4	0.0
Model IV	23.3	31.9	26.2
Model V	14.6	7.2	0.0

transition state of this step lies 7.5 kcal/mol above **MIV** (Fig. 11), which indicates an efficient hydrolysis step.

The extradiol reaction paths proceeds in a very similar manner to that found for model I and II. For the transition state of this step, i.e. **TM2** (Figure S12a), which lies 7.2 kcal/mol above **M2**, the C–C bond is stretched to 2.42 Å (Table 1). Extending this bond length to 3.08 Å leads to the extradiol C–C bond cleavage product – **M3** (Figure S 12b), which is 3.9 kcal/mol less stable than the alkoxyl radical **M2**. The acyclic organic radical that is a part of **M3** possesses an unpaired electron on carbon C2, which is reflected in spin population of −0.98. Subsequently, in the ultimate step of this path, the hydroxyl ligand attacks the radical carbon C2 leading to the final product of this reaction, i.e. **M4**. The activation barrier of this hydroxylation is 6.6 kcal/mol (Fig. 11).

In summary, the results obtained for the model V confirm the observation that protonation of the peroxo group lowers the energy barrier for homolytic O–O bond cleavage. Like for the models I and II, it was found that the reaction mechanism for intradiol path is favorable.

3.1.3.1. Models III, IV compared to models I, II and V

Investigations for the models III, IV confirm the major conclusions which were derived from the results obtained for the models I, II and V. Namely, in the models featuring the protonated peroxo group (the models I, III and V, Figs. 4 and 5) the barrier for O–O bond cleavage is substantially lower than for the model with this group deprotonated, i.e. the barrier is 12.9, 15.3, 14.6 and 23.6, 23.3 kcal/mol for the models I, III, V and II, IV, respectively (Table 2). Notably, for the models with the protonated peroxide the products of the O–O bond cleavage do not involve the oxoferryl species, but instead the tyrosine ligand is oxidized to the tyrozyl radical, like for one of the mechanisms suggested for the native reaction of intradiol dioxygenases (**d′** → **e′** → **f**, Fig. 2). Moreover, for all models considered here the alkoxyl radical, which results from O–O bond scission, preferably decays through the intradiol type cleavage. The energies of the transition states for intradiol and extradiol cleavage are the following: 9.4 and 21.2 kcal/mol for the model III, 24.2 and 29.9 kcal/mol for the model IV (Table 2). Thus, the energetic preference for the intradiol channel ranges from 3.2 (the model I) to 11.8 kcal/mol (the model III), which can be compared to the value of 9.1 kcal/mol calculated for the free alkoxide radical derived from **A**.

Due to the fact that the models II and III are related to each other by a proton transfer between the hydroperoxo group and the OH ligand and a release of the thus formed water molecule, for these two models it is possible to calculate the activation energies with respect to the same reference point (**RI**). Such a comparison reveals that the barrier for the O–O bond cleavage in the model III is 18.5 kcal/mol, whereas in the model II it amounts to 23.6 kcal/mol, i.e. 5.1 kcal/mol more. Therefore, the barrier for the cleavage of the O–O bond is indeed considerably reduced when the peroxide group is protonated, which is an observation also made in the previous theoretical study on the intradiol dioxygenase reaction with the native substrate[11]. For the products of the O–O bond cleavage, i.e. the alkoxyl radical/oxidized iron cofactor intermediate, the energetic preference for the model with the protonated peroxide is reduced to 2 kcal/mol.

4. Conclusions

The reaction mechanism for the intradiol dioxygenase and the probe substrate **A** (Fig. 3) was investigated with the quantum chemical method B3LYP employing five different models of the active site region in the enzyme–substrate complex. The models differ in the total charge and the number of endogenous ligands, yet the results obtained for them converge to several major conclusions. Specifically, the presence of the proton bound to the peroxo group markedly lowers the activation barrier for the critical O–O bond cleavage step. Importantly, the lower-barrier path does not lead to the oxoferryl species, but instead to the Fe^{III}–OH complex with one of the tyrosine residues oxidized to the tyrozyl radical. Therefore, it is very probable that the alkoxyl radical is generated without forming the very reactive oxoferryl species, contrary to the mechanism previously proposed, which is presented in Fig. 3. Moreover, cleavage of the ring in the alkoxyl radical intermediate **B** (Fig. 3) preferentially leads through the intradiol path, which is consistent with the larger stability of the resulting product. However, this observation contrasts with the experimental finding that the extradiol cleavage product is observed. Taking into account the 9.1 kcal/mol preference of the alkoxyl radical to decompose through the intradiol path, it seems plausible that some very specific steric hindrance is present in the active site of the intradiol dioxygenase, and that it reverts the chemospecificity of the ring cleavage reaction for the probe **A**. Unfortunately at the present stage there is not enough data on the actual binding mode of the probe within the active site, and thus it is very hard, if not impossible, to model the reaction at the required level of accuracy to explain the observed product specificity. X-ray and/or spectroscopic data, providing insights into the structure of the enzyme – **A** complex, are the prerequisites of such high-accuracy modeling studies.

Acknowledgements

We want to thank the Polish State Ministry of Science and Higher Education (MNiSW) for supporting this research project from the funds for scientific research (grant N301 093036). This work was sponsored by the "Krakow Interdisciplinary PhD-Project in Nanoscience and Advanced Nanostructures" operated within the Foundation for Polish Science MPD programme co-financed by the EU European Regional Development Fund.

Appendix A. Supplementary data

Supplementary data associated with this article can be found, in the online version, at doi:10.1016/j.cattod.2010.08.028.

References

[1] C.K. Brown, M.W. Vetting, C.A. Earhart, D.H. Ohlendorf, Annu. Rev. Microbiol. 58 (2004) 555–585.
[2] M. Costas, M.P. Mehn, M.P. Jensen, L. Que, Chem. Rev. 104 (2004) 939–986.
[3] O. Hayaishi, M. Katagiri, S. Rothberg, J. Am. Chem. Soc. 77 (1955) 5450–5451.
[4] M.W. Vetting, D.H. Ohlendorf, Structure 8 (2000) 429–440.
[5] D. Ohlendorf, A. Orville, J. Lipscomb, J. Mol. Biol. 244 (1994) 586–608.

[6] M.P. Valley, C.K. Brown, D.L. Burk, M.W. Vetting, D.H. Ohlendorf, J.D. Lipscomb, Biochemistry 44 (2005) 11024–11039.
[7] A. Orville, N. Elango, J. Lipscomb, D. Ohlendorf, Biochemistry 36 (1997) 10039–10051.
[8] C.A. Tyson, J. Biol. Chem. 250 (1975) 1765–1770.
[9] G.P. Horsman, A. Jirasek, F.H. Vaillancourt, C.J. Barbosa, A.A. Jarzecki, C. Xu, Y. Mekmouche, T.G. Spiro, J.D. Lipscomb, M.W. Blades, R.F.B. Turner, L.D. Eltis, J. Am. Chem. Soc. 127 (2005) 16882–16891.
[10] T. Funabiki, T.J. Yamazaki, Mol. Catal. A 150 (1999) 37–47.
[11] T. Borowski, P.E.M. Siegbahn, J. Am. Chem. Soc. 128 (2006) 12941–12953.
[12] M. Xin, T.D.H. Bugg, J. Am. Chem. Soc. 130 (2008) 10422–10430.
[13] N. Nakatani, Y. Nakao, H. Sato, S. Sakaki, J. Phys. Chem. B 113 (2009) 4826–4836.
[14] V. Georgiev, H. Noack, T. Borowski, M.R. Blomberg, P.E.M. Siegbahn, J. Phys. Chem. B 114 (2010) 5878–5885.
[15] A.D. Becke, J. Chem. Phys. 98 (1993) 5648–5652.
[16] C. Lee, W. Yang, R.G. Parr, Phys. Rev. B37 (1988) 785–789.
[17] JAGUAR 7.6, Schrödinger, Inc., Portland, OR, 2009.
[18] Gaussian 09, Revision A.1, M.J. Frisch, G.W. Trucks, H.B. Schlegel, G.E. Scuseria, M.A. Robb, J.R. Cheeseman, G. Scalmani, V. Barone, B. Mennucci, G.A. Petersson, H. Nakatsuji, M. Caricato, X. Li, H.P. Hratchian, A.F. Izmaylov, J. Bloino, G. Zheng, J.L. Sonnenberg, M. Hada, M. Ehara, K. Toyota, R. Fukuda, J. Hasegawa, M. Ishida, T. Nakajima, Y. Honda, O. Kitao, H. Nakai, T. Vreven, J.A. Montgomery, Jr., J.E. Peralta, F. Ogliaro, M. Bearpark, J.J. Heyd, E. Brothers, K.N. Kudin, V.N. Staroverov, R. Kobayashi, J. Normand, K. Raghavachari, A. Rendell, J.C. Burant, S.S. Iyengar, J. Tomasi, M. Cossi, N. Rega, J.M. Millam, M. Klene, J.E. Knox, J.B. Cross, V. Bakken, C. Adamo, J. Jaramillo, R. Gomperts, R.E. Stratmann, O. Yazyev, A.J. Austin, R. Cammi, C. Pomelli, J.W. Ochterski, R.L. Martin, K. Morokuma, V.G. Zakrzewski, G.A. Voth, P. Salvador, J.J. Dannenberg, S. Dapprich, A.D. Daniels, Ö. Farkas, J.B. Foresman, J.V. Ortiz, J. Cioslowski, D.J. Fox, Gaussian, Inc., Wallingford CT, 2009.
[19] D.J. Tannor, B. Marten, R. Murphy, R.A. Friesner, D. Sitkoff, A. Nicholls, M. Ringnalda, W.A. Goddard III, B. Honig, J. Am. Chem. Soc. 116 (1994) 11875–11882.
[20] B. Marten, K. Kim, C. Cortis, R.A. Friesner, R. Murphy, M. Ringnalda, D. Sitkoff, B. Honig, J. Phys. Chem. 100 (1996) 11775–11788.